Journal of Power Sources 564 (2023) 232804

Contents lists available at ScienceDirect

Journal of Power Sources

journal homepage: www.elsevier.com/locate/jpowsour

Multi-modal characterization methods of solid-electrolyte interphase in silicon-graphite composite electrodes

Zoey Huey [a,b], Yeyoung Ha [a], Sarah Frisco [a], Andrew Norman [a], Glenn Teeter [a], Chun-Sheng Jiang [a], Steven C. DeCaluwe [b,*]

[a] National Renewable Energy Laboratory, 15013 Denver West Parkway, Golden, CO, 80401, USA
[b] Colorado School of Mines, 1500 Illinois Street, Golden, CO, 80401, USA

HIGHLIGHTS

- Multi-modal imaging shows a bilayer SEI structure on silicon-graphite electrodes.
- Most Li deposited in the SEI is in the form of LiF.
- LiF concentration in the SEI is proportional to maximum SEI resistivity.
- XPS shows an inverse relationship between Li_2CO_3 and LiF in the SEI composition.
- Data discrepancies arise from varying depth and spatial resolution of the techniques.

ARTICLE INFO

Keywords:
Solid electrolyte interphase
Surface characterization
Silicon electrodes
Lithium ion batteries

ABSTRACT

Composite silicon-graphite (Si-Gr) anodes can improve battery energy density, due to Si's high gravimetric capacity, while mitigating mechanical degradation of the anode and solid-electrolyte interphase (SEI) caused by Si volumetric expansion. Optimizing these anodes is challenging, in part due to difficulty characterizing the SEI structure and composition. In this work, we present multi-modal characterization of the SEI on composite Si-Gr anodes to relate SEI chemical composition and structure to functional properties. Discrepancies in elemental concentrations from X-ray photoelectron spectroscopy, Auger electron spectroscopy, and energy-dispersive X-ray spectroscopy (EDS) are attributed to varying information depth and lateral resolution of the individual probes. However, by combining quantitative composition information with spatially resolved element mapping from scanning transmission electron microscopy, EDS, and electron energy loss spectroscopy, a holistic picture of the SEI emerges. We observe the bilayer SEI structure and a direct correlation between elemental Li and F, suggesting that most Li in the SEI exists as lithium fluoride (LiF). Further, LiF concentration is directly proportional to the maximum SEI resistivity, as determined by scanning spreading resistance microscopy. Lastly, there is an inverse relationship between lithium carbonate and LiF concentration in the SEI, providing insight into the detailed chemistry of SEI formation and evolution.

1. Introduction

As efforts to decarbonize the transportation sector become more widespread, there is a need for lighter electric vehicle (EV) batteries to facilitate rapid commercialization [1]. Silicon (Si) as an anode material has much greater theoretical capacity (3579 mAh g_{Si}^{-1}) than the more standard graphite material (Gr, 372 mAh g_{Gr}^{-1}) [2,3]. However, Si undergoes large volumetric changes during cycling, which results in mechanical instability of both the active material and the associated solid-electrolyte interphase (SEI). The SEI is an electron-insulating, Li^+ ion-conducting layer that forms on the electrode surface due to electrolyte reduction occurring at low anode potentials [4]. An effective SEI is a critical factor in determining the anode performance, as it provides passivation against continued electrolyte decomposition during cycling. However, in Si anodes, the volumetric changes that occur during cycling damage the SEI and form new SEI on the freshly exposed Si material,

* Corresponding author.
E-mail address: decaluwe@mines.edu (S.C. DeCaluwe).

https://doi.org/10.1016/j.jpowsour.2023.232804
Received 2 November 2022; Received in revised form 30 January 2023; Accepted 8 February 2023
Available online 2 March 2023

which consumes Li and results in sustained capacity fade over the battery lifetime [5–7].

Although using pure Si would provide maximum electrode capacity, due to its (electro)chemical and mechanical instability, small amounts of Si are instead added to Gr electrodes to increase the energy density while mitigating mechanical issues [8]. Composite electrodes, made of active material particles of multiple phases held together with a binder, have been studied in a variety of electrode systems as a means of retaining the advantageous properties of the constituent active phases [9–11]. Indeed, composite Gr-Si anodes have reduced capacity fade and reduced manufacturing costs compared to pure Si anodes [2,5]. However, the Si content is typically kept under 33 wt%, resulting in a specific capacity of only ~1300 mAh $g^{-1}_{Electrode}$, far below the theoretical limit of pure Si [12,13]. To improve electrode capacity and therefore EV efficiency and range, it is necessary to increase the Si content, and with this comes a need to understand and address factors that limit durability in Si and composite electrodes, such as SEI instability and poor calendar life [14,15].

A stable SEI is key to supporting extended cycle and calendar life for batteries. An effective SEI should cover the electrode surface and prevent electron transfer that causes deleterious electrolyte reduction reactions at low anode potentials during charging, while still maintaining a Li^+ ion conducting pathway [16]. However, the influence of various SEI species, such as lithium fluoride (LiF) and lithium carbonate (Li_2CO_3), on key properties (e.g., resistivity) and performance metrics (e.g., long-term capacity fade) are not well understood [17–19]. The mechanisms that form these compounds and the ways that cycling conditions and electrolyte composition impact SEI properties are also debated. These uncertainties have hindered scientifically guided design of the battery SEI to optimize cell performance in Si and composite Si-Gr anodes. For example, it is generally agreed that fluoroethylene carbonate (FEC) as an electrolyte additive improves cell performance, but the mechanism and its exact impact on the SEI is debated [20,21]. The lack of consensus on SEI formation, chemistry, and ideal properties means that there is a need for comprehensive characterization methods to study the SEI and its characteristics to further improve electrode performance. By obtaining data on characteristics such as the chemical compounds present in the SEI, we can better understand how degradation occurs in the electrolyte. This data, when correlated to electrochemical data and information on properties such as resistivity, will allow us to analyze the impacts of SEI compounds and optimize performance.

However, characterizing SEI morphology, composition, and evolution in composite anodes is non-trivial. Much previous SEI characterization work has been conducted on model thin-film or wafer electrodes; this approach provides an ideal sample for many techniques but does not fully represent a composite system [7,22–24]. In composite systems, the SEI forms in a layer around all the electrode active particles, creating a three-dimensional structure with a rough surface [25]. The spatial distributions of the multiple phases, which exist at disparate length scales, are difficult to deconvolute, and the system only increases in complexity during cycling, when electrolyte degradation occurs, multicomponent and heterogenous SEI forms and evolves, and active material reacts with Li^+ ions (i.e., intercalation, alloying).

Many of the techniques used to study the SEI have a fixed sampling volume (i.e., surface vs. bulk sensitive, detection area) and spatial resolution, and therefore are limited in their ability to characterize the complex three-dimensional structure of the SEI and capture heterogeneity within the SEI. Each technique serves a unique purpose, and no single technique can fully characterize the SEI, particularly in a composite system. Analysis techniques such as X-ray photoelectron spectroscopy (XPS) and Auger electron spectroscopy (AES) identify compounds and species close to the sample surface [26,27]. However, in a composite electrode with a complex three-dimensional SEI of varying thickness, these techniques may not fully characterize the SEI. Scanning transmission electron microscopy (STEM) uses a cross-sectional sample to fully analyze the whole SEI, but this technique involves difficult sample preparation and instrument operation, and is more limited in terms of chemical characterization [28]. Scanning probe-based scanning spreading resistance microscopy (SSRM) can measure SEI resistivity, but not composition [25,29]. A more complete understanding of the SEI and how to improve it requires a combination of techniques.

In this paper, we present a combined analysis of multiple characterization methods—including STEM, energy-dispersive X-ray spectroscopy (EDS), electron energy loss spectroscopy (EELS), AES, XPS, and SSRM—to study the SEI in composite Si-Gr electrodes. Combined, these techniques provide information on the SEI's elemental composition and spatial distribution, chemical composition, and electrical resistivity. We discuss the strengths and limitations of each technique and demonstrate how combined analysis provides insights that exceed those provided by any single technique. By studying two different electrolyte systems (with and without FEC additive) cycled at two different temperatures, we demonstrate how to analyze and relate elemental and chemical composition, spatial component distribution, and electronic resistivity. We also demonstrate a possible trade-off between the amounts of LiF and Li_2CO_3, as well as a link between maximum SEI resistivity and LiF content.

2. Methods

A range of chemical and elemental analysis techniques are utilized in battery research, each with strengths and limitations [30]. Many of these techniques, although not all, are surface sensitive, as the electrode interfaces and the SEI layer are of particular interest. In this study, we analyze a Si-Gr composite anode, combining multiple techniques for a holistic view of the SEI morphology, composition, and electrical resistivity as a function of electrolyte composition and battery cycling conditions. The composite anode structure and an overview of the techniques used here are presented in Fig. 1.

The composite anode, consisting of Gr, Si, conductive carbon particles, and binder, forms a three-dimensional SEI structure when cycled, as shown in Fig. 1(a) and (b). The binder is not depicted, as it is ideally distributed uniformly around all particles and is not (electro)chemically active. For the sake of clarity and generalizability to other composite electrodes, the particles are shown as idealized spheres and are not to relative scale [14]. The complex SEI structure, coupled with the rough surface that often results from larger (micron-scale) particles, means that surface analysis must be done carefully. We take into consideration the interaction depth of each technique, as the analysis volume could consist of either only SEI or SEI plus active material. Even if the depth is shallow enough that only SEI is studied, the composition can vary based on the underlying active material or a spatially heterogeneous SEI. We also consider the spot size to determine whether the interrogated volume/surface is a representative average or whether it varies with the location of the probe.

2.1. Characterization techniques: strengths and limitations

We begin with a short summary of the techniques used herein. STEM (Fig. 1(c)) works by rastering a focused, small-diameter (typically <1 nm) electron probe to image a sample while also identifying and spatially mapping individual elements through techniques such as EDS and EELS [28]. A spatial elemental map provides insight into where the SEI forms, and what morphology and composition changes might occur during cycling. Unlike the other techniques herein, STEM is not strictly surface sensitive; rather, it is carried out on a very thin (electron transparent) cross-sectional sample that has been extracted from the electrode using focused ion beam (FIB) techniques. STEM collects images containing both SEI and composite active particles. EDS measures the energy of X-rays emitted by the sample, with a known characteristic energy for each element [28]. The number of X-ray counts for one element relative to another provides quantitative concentration analysis. EELS measures the energy lost by the incident beam electrons after

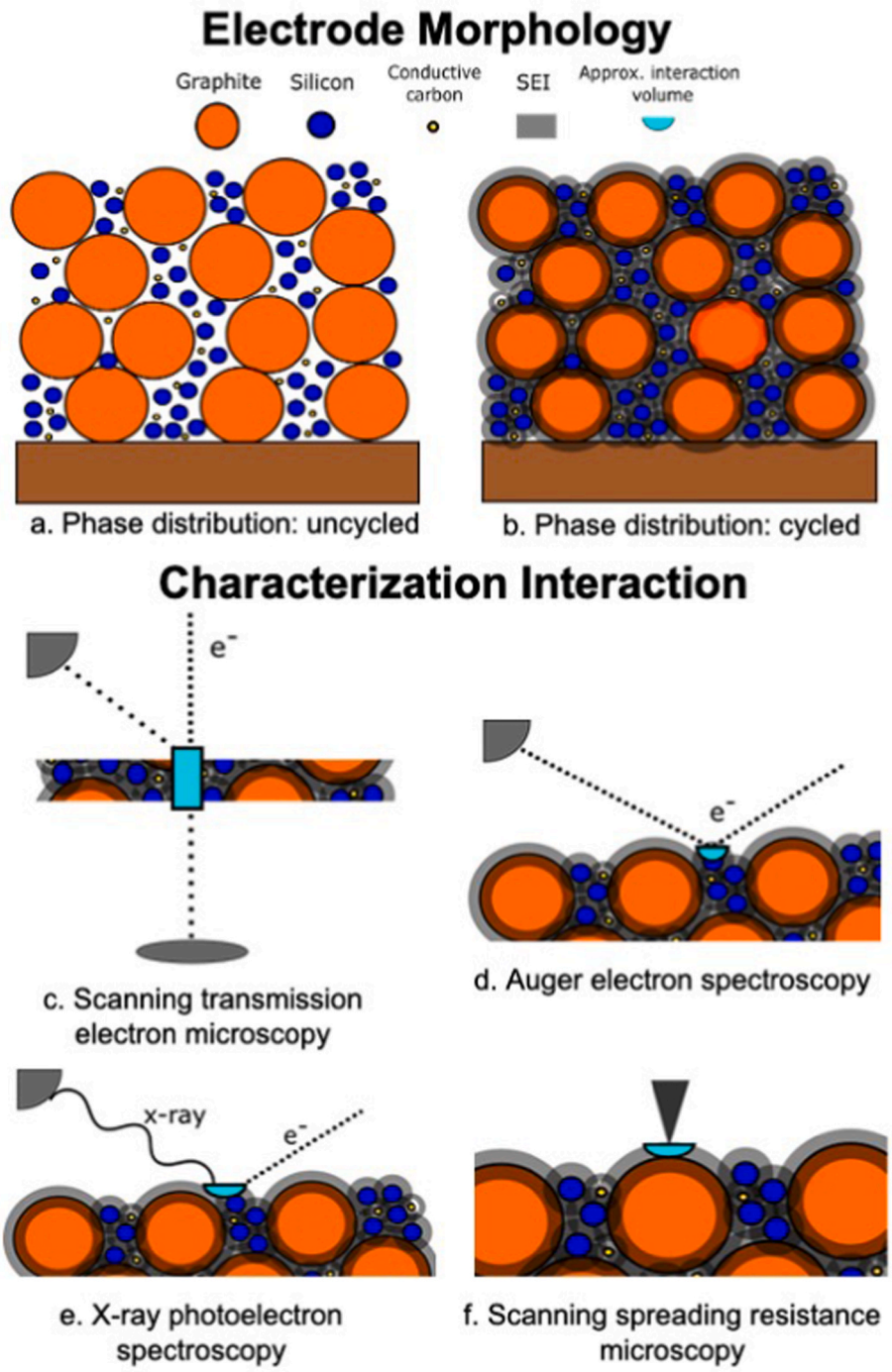

Fig. 1. Schematic diagrams of (a) the phase distribution of a composite electrode with multiple particle sizes (note that binder is not represented for the sake of clarity, as binder content is typically low), (b) SEI formation on the same composite electrode, (c) STEM interaction with a cycled composite electrode sample, (d) AES interaction with the sample, (e) XPS interaction with the sample, and (f) SSRM interaction with the sample.

they experience inelastic collisions in the sample [28]. EELS is generally better than EDS for measuring light elements that don't emit as many X-rays, such as Li. It also has high spatial resolution; typical operating settings can provide a resolution of 25 nm, but higher resolution can be achieved with thinner samples or aberration corrected instruments [31]. In general, access to STEM instruments is limited and requires extensive training. Sample preparation is also challenging and time consuming, especially with air- and moisture-sensitive composite electrodes [28].

AES (Fig. 1(d)) is highly surface sensitive and therefore valuable for studying SEI—it has a typical information depth of 5–10 nm and is capable of measuring only the SEI and not the underlying electrode material (assuming that the SEI is nonporous) [26]. AES measures the intensity of Auger electrons emitted when a sample is bombarded by an electron beam. The spot size is on the order of 10 nm, providing highly localized composition information. AES determines elemental composition and can create area maps when used in scanning mode. One challenge that arises when performing AES on a resistive sample, such as a cycled electrode with a resistive SEI, is charging due to electrons remaining on the sample, which impacts image resolution. A related issue is that the electron current injected into the sample during AES can cause Li^+ ion migration, which in turn alters surface composition.

XPS (Fig. 1(e)) is a widely used characterization method that

quantifies elemental composition and chemical states at the sample surface [27]. XPS bombards a sample with X-ray photons (typically Al kα, where hν = 1486.7 eV) and measures the intensity of the core-level photoelectrons emitted by the sample as a function of binding energy. XPS provides information about composition and chemical states present in a sample through core-level peak areas and binding energy shifts, respectively. Correlations between binding energy separations and peak areas for various elemental core levels can help identify specific chemical phases that are present in the sample [32]. XPS is surface sensitive, as emitted electrons cannot travel very far through the sample, with an information depth of approximately 5–10 nm [27]. By quantifying the chemical species present at the sample surface, XPS can provide insight into the SEI's chemical composition and the specific degradation reactions that formed it. XPS spot size is typically on the order of tens to hundreds of microns, providing electrode-scale average compositions. XPS analysis of the SEI requires accurate interpretation of binding energy shifts, which can be challenging due to the impact of sample-charging effects on low-conductivity samples. However, instruments with a charge neutralizer can mitigate charging. Many phases in LiB SEIs have overlapping XPS peaks, further complicating data interpretation [32]. Additionally, the X-ray photons in XPS can damage the SEI and change its composition during measurement, unless care is applied to control overall X-ray fluence in a particular measurement area on the sample.

SSRM (Fig. 1(f)), a form of scanning probe microscopy, collects localized, nm-scale Ohmic resistivity by placing a probe with a nominally 30-nm tip radius in contact with the sample and forming a circuit between the sample and the instrument with a constant voltage bias [25,33]. The use of a logarithmic amplifier to measure small changes in resistance, coupled with the small size of the tip, allows SSRM to measure the local surface resistivity, providing the resistivity of the phases present and their spatial distributions. The surface resolution is limited to the diameter of the probe tip, and the interaction depth is similar to the probe size. An effective SEI passivates the active electrode material, blocking undesirable parasitic electrochemical reactions, so electronic resistivity is a desirable attribute [16,30,34]. SSRM can offer insight into SEI quality that becomes especially powerful when paired with elemental characterization techniques. SSRM measures the resistivity of the SEI with high lateral resolution, and is also capable of measuring complex composite systems, in contrast to commonly used techniques such as four probe measurement, which typically measure thin films [34]. Previously, SSRM was used by this research group to identify the individual components in Si-Gr composite anodes, via the intrinsic resistivities of each component [35]. However, when these electrodes are cycled, the components react and degrade, and SEI forms on the active material particles [36,37]. The resulting shift in component resistivities makes it more complicated to identify the components in the anode through SSRM alone.

2.2. Electrode sample preparation

Here, we present an analysis of four Si-Gr electrode samples produced by the Cell Analysis, Modeling and Prototyping (CAMP) facility at Argonne National Laboratory. The electrode slurry, containing 15 wt% Paraclete Energy Si nanoparticles (average diameter 150 nm), 73 wt% Hitachi MagE3 graphite (average diameter 20 μm), 2 wt% TIMCAL C45 conductive carbon, and 10 wt% lithium polyacrylate (LiPAA) binder, was coated on a 10 μm copper (Cu) foil with 3.0 mg/cm^2 coating loading, with a calendered thickness of 37 μm. The electrode was dried at 150 °C under vacuum prior to use. The electrolytes used were:

- Gen2 – 1.2 M lithium hexafluorophosphate ($LiPF_6$) in ethylene carbonate (EC): ethyl methyl carbonate (EMC) (3:7 by wt%)
- GenF – Gen2 with 10 wt% FEC additive

Half-cells were prepared in an argon (Ar)-filled glove box using a 2032-type coin cell format—consisting of 14-mm-diameter Si-Gr electrode, 19-mm-diameter Celgard 2325 separator, and 15.5-mm-diameter Li metal (Alfa Aesar, 99.9%, 0.75 mm thick) electrode—with 40 μL electrolyte. The coin cells were cycled at a rate of C/20 for the first three cycles, and then C/3 for the next 22 cycles, for a total of 25 cycles The cycling voltages ranged from 0.05 to 1.5 V vs. Li/Li$^+$. 3.68 mA was applied as 1C rate current. Two cells of each electrolyte (Gen2 and GenF) were cycled in temperature-controlled chambers, one set held at 25 °C and the other held at 70 °C. Electrochemical cycle data is shown in Fig. S1, which agrees well with previously reported results [38].

After the 25 cycles were completed, the cells were electrochemically delithiated and disassembled in the glove box and the retrieved electrodes were soaked in dimethyl carbonate (DMC) for 60 s to remove residual electrolyte. Then, the electrodes were dried under dynamic vacuum for 30 min prior to performing surface characterizations.

2.3. Characterization details

XPS results were collected using a Physical Electronics VersaProbe III with a base pressure below 2×10^{-9} Torr. The samples were mounted in an Ar glovebox and transferred in a sealed vessel to the AES, preventing any atmospheric exposure. Monochromatic Al Kα X-ray excitation (hν = 1486.7 eV) was used to generate photoelectrons. The binding energy (BE) values were calibrated using the core-level spectra of sputter-cleaned Au and Cu foils (Au 4f7/2 = 83.96 eV and Cu 2p3/2 = 932.62 eV) [39]. On each sample, a single 100 μm square area was analyzed.

STEM samples were prepared using an FEI Nova NanoLab 200 dual-beam FIB workstation. FIB lift-out samples were prepared using 30-kV Ga$^+$ ions, with the sample surface protected first with platinum (Pt). Final FIB milling was performed with <5-kV Ga$^+$ ions to minimize sample damage. STEM-EDS and STEM-EELS data were gathered using an FEI F20 UltraTwin field emitting gun STEM operated at 200 kV. EDS results were obtained using an EDAX Octane T Optima windowless 60-mm^2 silicon drift detector EDS system. EELS data were obtained using a Gatan Model 977 Enfinium ER EELS system. Samples were transferred from an Ar glovebox to FIB to STEM via an air-free transfer system and an air-free TEM sample holder.

AES and scanning Auger microscopy (SAM) results were collected using a Physical Electronics 710 AES with a base pressure lower than 3×10^{-10} Torr. Samples were transferred into the instrument using the same atmosphere-free method as XPS. The beam energy was 5 kV, and the beam current was 10 nA. The ion gun's charge neutralizer setting was used on these samples to prevent charging.

SSRM measurements were collected using a Veeco Dimension 5000 system fitted with a Bruker SSRM module installed in an Ar glovebox. Conductive diamond-coated Si probes (Bruker DDESP-V2) were used for SSRM scans, and a −0.25 V bias was used to avoid potential lithium plating.

Details for data processing for all the above techniques can be found in the Supplementary Information.

3. Results

3.1. XPS

The C 1s, O 1s, P 2p, and F 1s XPS spectra and fittings for all four Si-Gr samples are shown in Fig. 2. LiF was detected by XPS in all Si-Gr samples; Gen2 at 70 °C had the most; GenF at 70 °C and 25 °C had similar amounts; and Gen2 at 25 °C had the least. Li_2CO_3 was also detected in all four samples; the GenF samples had similar amounts at high and low temperatures, whereas the Gen2 at 70 °C had the smallest amount and the Gen2 at 25 °C had the largest amount. These data indicate an inverse relationship between the relative amounts of LiF and Li_2CO_3 in each sample. Results show greater amounts of Li_xPO_y in the electrodes cycled at 70 °C relative to 25 °C, and greater amounts of

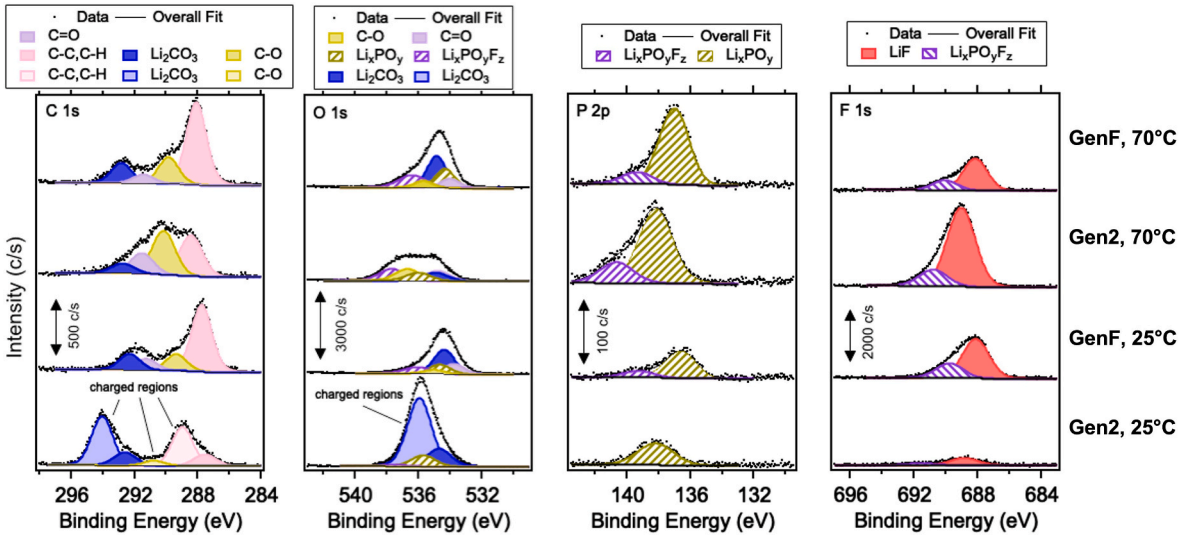

Fig. 2. XPS results for four samples showing P 2p, C 1s, O 1s, and F 1s core-level spectra. Differential surface charging occurred in the Gen2 25 °C sample and the resulting peak shifts are indicated.

$Li_xPO_yF_z$ when cycling in Gen 2 electrolyte relative to Gen F electrolyte. The amounts of both Li_xPO_y and $Li_xPO_yF_z$ follow the same trends relative to LiF.

3.2. STEM-EDS and EELS

In the EDS images shown in Fig. 3(a), F appears concentrated closer to the active particles, and other elements, like C, show a greater density near the SEI surface. The maps from the Gen2 at 70 °C sample are shown in Fig. 3 as an example; EDS maps for the other samples can be found in Fig. S3. The EELS images show some clustering of elements and compounds, particularly F and Li, which is discussed in more detail in the next section. However, there is also a more uniform distribution of O and C, as well as Li in some areas. Although O and C are both present in the electrode materials, by referencing the Si location and the C density, we can get a general idea of what is SEI and what is active material. We can also qualitatively show that electrode components other than LiF are well distributed at this length scale.

3.3. SSRM

Resistivity values from SSRM mapping of the sample surface are shown in Fig. 4. The average SEI resistivity values were similar, with Gen2 at 70 °C having greater resistivity than Gen2 at 25 °C, and both GenF samples having similar resistivities. The maximum resistivity values for each sample varied more, with Gen2 at 70 °C having the highest value, then GenF at 70 °C, then GenF at 25 °C. Gen2 at 25 °C had the lowest maximum resistivity. There is not a clear correlation between average and maximum resistivity values.

4. Discussion

4.1. Composition analysis

The quantitative elemental composition of the SEI is of interest because it offers insight into the degradation reactions that occur during cycling. The composition can be found through several different techniques; however, each has different sensitivities, interaction volumes, and uncertainties [27,40–42]. The uncertainty associated with each technique depends on the extent of calibration performed and the corrections done, as well as the capabilities of the individual instrument. This uncertainty should be taken into consideration when analyzing quantitative SEI composition data. In many cases, relative elemental

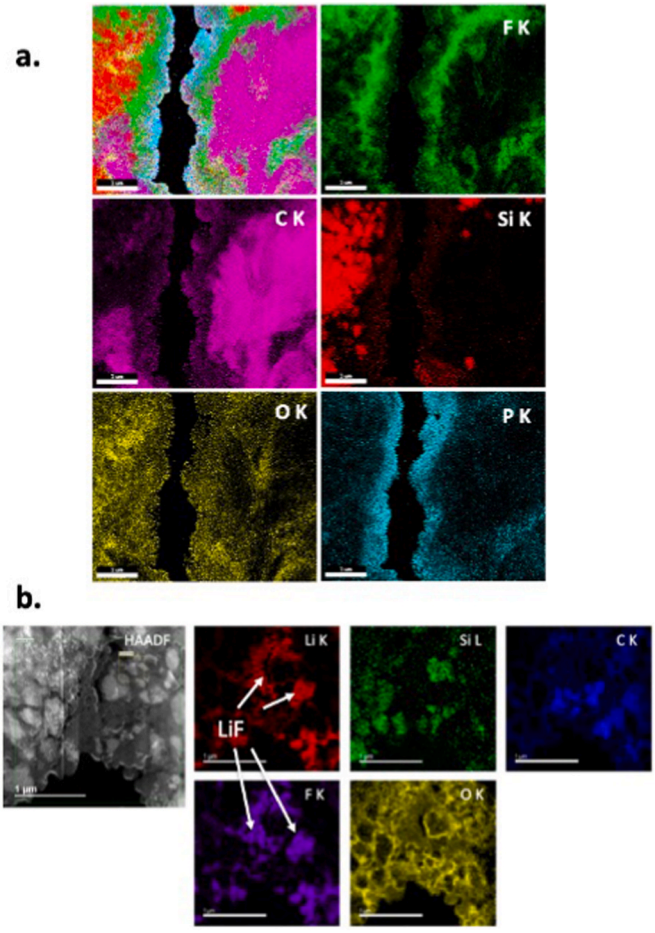

Fig. 3. (a) STEM-EDS maps from Gen2 at 70 °C showing SEI containing F, C, and O on both Gr and Si particles, with a separation between C and F indicating a possible bilayer. (b) STEM high-angle annular dark field (HAADF) and EELS maps of the sample with Gen2 at 70 °C, with clear overlap of Li and F in ~100-nm LiF particles.

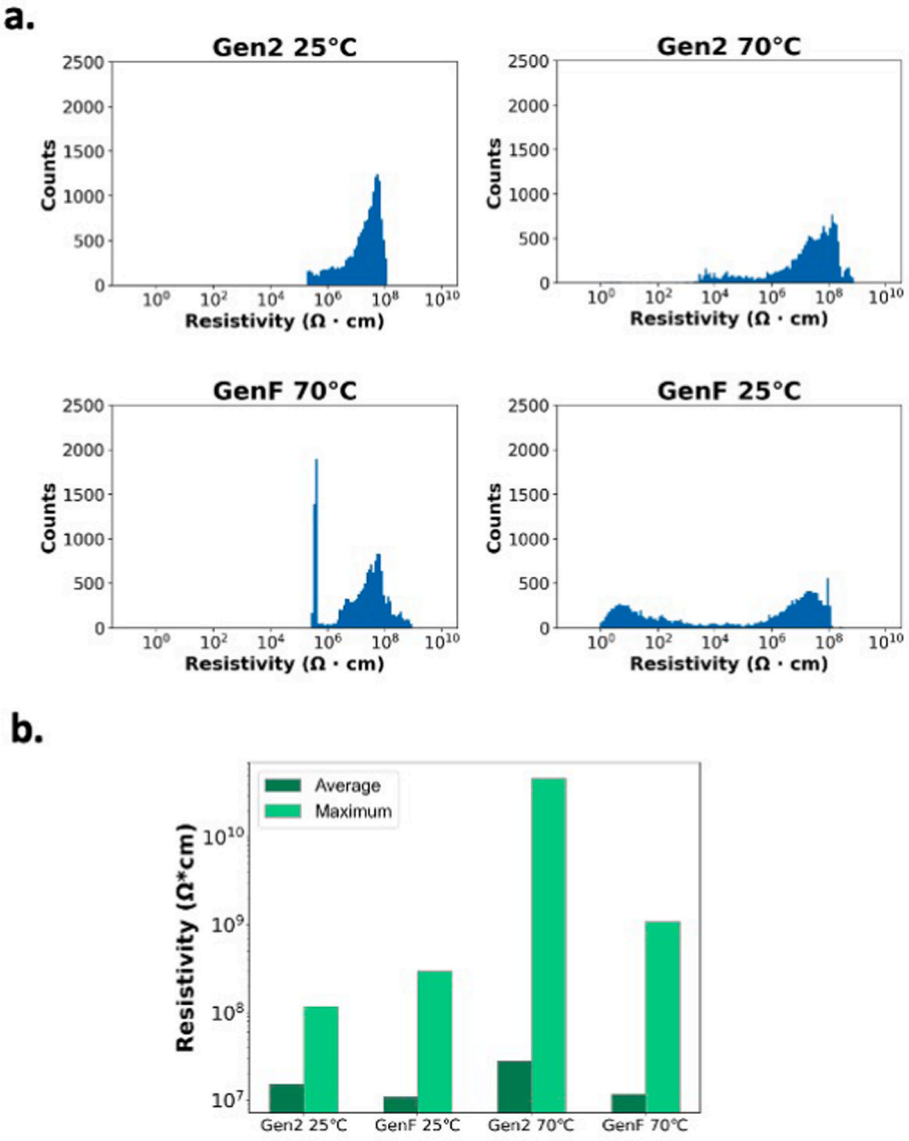

Fig. 4. (a) Histograms for surface SSRM data, showing the distribution of resistivity values for the SEI and the underlying active material. (b) Average and maximum SEI resistivity values for each sample from SSRM data. Average resistivities are similar, but the maximum resistivities vary more.

amounts are more instructive than absolute amounts, especially when comparing electrode samples cycled under different conditions. Using multiple characterization techniques provides a comprehensive understanding of SEI composition, but the high variability should be addressed.

Fig. 5 provides the relative molar concentrations (%) of selected SEI elements (carbon [C], oxygen [O], fluorine [F], and phosphorus [P]), as measured and calculated by STEM-EDS, AES, and XPS. In some cases, the three techniques measure markedly different compositions, likely due to differences in information depth, with no clear trends across the four samples. These discrepancies may also be the result of varying sampling volumes. The elements quantified here are of particular interest in SEI research, as they originate from the EC, EMC, and $LiPF_6$ in the electrolyte, as well as the FEC additive, and form documented compounds such as LiF, Li_2CO_3, LiOH and Li phosphates and phosphides [30]. Although hydrogen is expected to be present in various SEI phases, it cannot be directly detected by the techniques used here.

STEM-EDS is conducted on a sample cross section, so it measures the entirety of the SEI, as well as the active Gr and Si particles. This affects the trends in the composition data and should be taken into consideration. A significant amount of Si was measured, as expected—between 17.6 and 33.2 atomic %. Si is not observed in XPS and AES, which implies complete coverage by the SEI. EDS measured more C than XPS did in all samples, but when compared to the AES data, this relationship is less consistent. The Gr particles imaged in EDS may account for the higher amount of C, as XPS does not penetrate through the SEI to these particles. AES has a different sensitivity to C than EDS does, which is discussed in depth in the following paragraph and may account for inconsistent trends in the C data. EDS also shows less O than both other techniques; this is likely due to the cross-sectional nature of the samples, as more of the analyzed area is not SEI and therefore contains less O. The P percentage is much higher in EDS than in AES and XPS and was thus not considered in this study. This discrepancy is due to the Pt commonly used in STEM sample preparation by FIB. The Pt and P EDS peaks cannot readily be distinguished; thus, Pt is erroneously measured as P, falsely increasing the percentage. A small amount of Pt was also identified in EDS, but not in AES or XPS. The AES and XPS data showed only small amounts of P, and there were no large areas of P identified in the EDS data. For these reasons, the STEM-EDS quantification data is presented in Fig. 5 with Pt, Si, and P removed and C, O, and F renormalized to

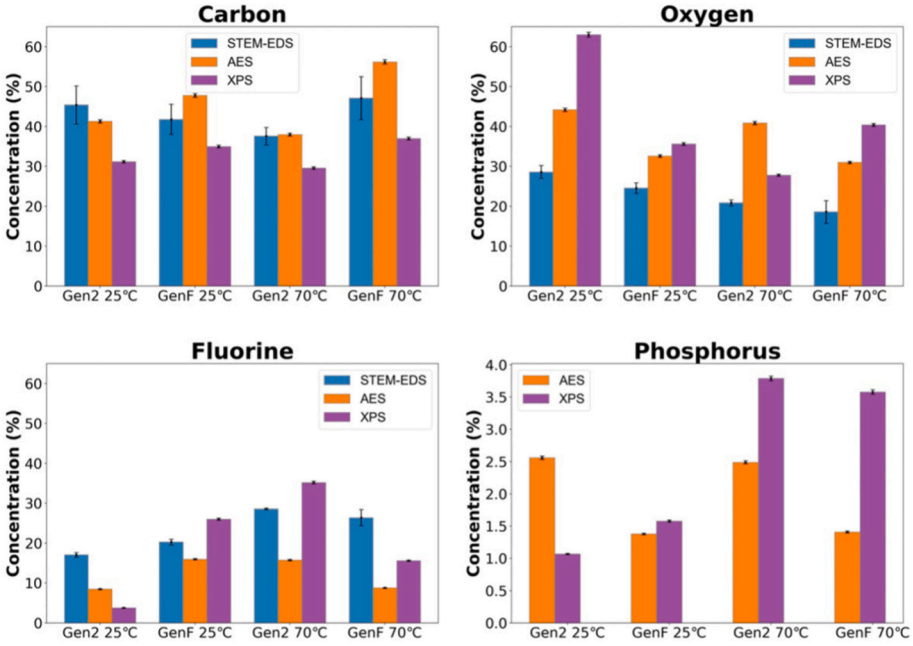

Fig. 5. SEI elemental composition for carbon (C), oxygen (O), fluorine (F), and phosphorous (P), as measured for the four cells by STEM-EDS, AES, and XPS. Results show variation across all three techniques due to differences in the interaction depths and sensitivities of each instrument. Phosphorous is not measured with STEM-EDS due to peak overlap with Pt, which is used in sample preparation and results in falsely high values. Error bars for STEM-EDS are based on 5-6 separate images, to capture sample spatial heterogeneity. AES and XPS imaging were over large areas and already capture spatial heterogeneity. Error bars for these techniques represent 1% standard error of measurement, the instrument resolution.

provide the most direct comparison of compositional values across techniques.

AES provides quantitative elemental information by calculating concentrations from the Auger peak intensity [26]. The AES data collected showed no Si signal, indicating that an SEI of at least 10 nm had formed on the Si-Gr samples. This thickness is consistent with STEM-EDS maps, discussed in the next section. We therefore assume that the SEI covers all electrode materials, that only the SEI composition is measured, and that any C or O measured is part of the SEI. Like XPS, AES sensitivity depends on the element detected, the overall matrix composition, and the morphology of the measured surface. The difference in C amounts between AES and other techniques observed here is likely due to heterogeneity across the SEI, as each technique measured a unique portion of the sample. For AES, one 50-μm square SAM map with a spot size of approximately 10 nm was analyzed for each sample, whereas XPS analyzed 100-μm square areas, and STEM-EDS analyzed 2–5-μm-square areas. Additionally, C may segregate to the organic-rich outer SEI layer (discussed in more detail in the following section), whereas F is largely presumed to exist in the inorganic inner layer. AES and XPS have different inelastic mean free paths (IMFPs) for different elements and can thus detect different elements at different depths; for the elements in this study, the IMFPs are greater for XPS than for AES (see Table S1). It makes sense that AES data includes a greater amount of C and a lower amount of F than XPS, as XPS measures a larger portion of the SEI thickness. Although heavier elements can be difficult to differentiate in AES due to overlapping energy peaks, the elements analyzed in this study are easily distinguished from one another [43]. The error in the EDS data is calculated from data collected from 5 to 6 different sites on each sample. AES and XPS data was collected from much larger maps, so the 1% error was calculated through instrumental error.

The XPS composition values in Fig. 5 show the least agreement with the other two techniques, but the trends between samples are qualitatively like the AES data. As previously mentioned, XPS and AES have different IMFPs, which is one source of their differing composition measurements. However, it is still likely that the full depth of the SEI is not analyzed in Fig. 5. In a composite system with a three-dimensional SEI, where thickness depends on surface location, it is impossible to know how much of the SEI has been measured. It is noteworthy that the amount of F, which is the only element studied in all three techniques and is uniquely present in the SEI and not the electrode itself, exhibits the same composition trends across all three techniques.

Although elemental analysis is a necessary and useful intermediate step, insights into the compounds that comprise the SEI are required to understand electrolyte decomposition processes and relate parameters such as electrolyte additives to electrochemical performance. For example, LiF is known to be an important component in an effective SEI, yet its role and the processes leading to its formation are not well understood [17,19]. We do know that some of the F originates from the $LiPF_6$ salt present in the electrolyte, and FEC additive provides another potential source of F [44]. Although FEC is known to improve electrode performance, the mechanism for this improvement is not well understood; some studies have concluded that FEC increases the amount of LiF, while others have found the opposite [21,45]. As shown in the XPS spectra (Fig. 2), LiF was detected in all Si-Gr samples, both with and without FEC added to the electrolyte. At 25 °C, a higher concentration of LiF was detected when FEC was present, indicating that FEC was an additional source of LiF formation. However, the opposite was observed at 70 °C, where the Gen2 sample showed a significantly higher LiF signal in the absence of FEC. Such behavior can be attributed to the much more severe electrolyte decomposition taking place in the absence of FEC at elevated temperatures in half-cells [38]. Also shown in Fig. 2 is an inverse relationship between the amount of LiF and Li_2CO_3 at the SEI surface, indicating a possible inverse relationship between the compounds; thus, if one is desired for cell performance, then the chemistry should be modified to minimize the other. LiF content appears to affect SEI electronic resistivity, which is discussed in a later section. Based on this, creating a more resistive SEI can be accomplished by decreasing Li_2CO_3 and increasing LiF.

The P in the SEI originates from the $LiPF_6$ electrolyte salt, which forms $Li_xPO_yF_z$ and Li_xPO_y phases upon reduction. Determining the exact stoichiometries of these compounds requires a separate series of experiments and is beyond the scope of this work. XPS results show a similar trend in the amount of Li_xPO_y and the amount of LiF. Previous literature reports have shown a decrease in the amount of $Li_xPO_yF_z$ relative to Li_xPO_y after 400 cycles with the addition of FEC to electrolyte [18]. This trend is observed in our samples at 70 °C but not 25 °C. While there may be a link between phosphorous-containing SEI compounds and improved SEI stability, further investigation is required. The SEIs in composite electrodes are heterogeneous, but the XPS analysis area is much larger than the composite particle size (and comparable to or

larger than the other characterization techniques discussed here), so it is likely that the areas analyzed were representative of the overall SEI.

We note that the electrodes in this study were cycled in half-cells; in addition, the SEI speciation has contributions from the Li metal electrode, as electrochemical data showed it is unstable at 70 °C in the absence of FEC, which provides effective passivation layer [38]. Nonetheless, the characterizations performed on these electrodes and the correlations made among the different techniques are valid and provide valuable information.

4.2. Elemental location

Mapping techniques reveal elemental distributions over various length scales within the composite anode, correlating these distributions with morphology and depth. For example, STEM provides high-resolution elemental maps of a sample cross section, allowing for a visualization of the SEI variation normal to the active material surface. In the Si-Gr samples studied, the SEI thickness, identified by locating Li, F, O, and C in relation to the Si and Gr particles, varied from tens to hundreds of nanometers due to the range of particle sizes and shapes, as well as the proximity to other particles and pore space.

SEIs in LiBs are sometimes described as having bilayer structures, with organic compounds on the surface, closest to the electrolyte, and inorganic compounds closest to the electrode [46,47]. Other studies suggest a more mosaic-like structure, with grains of different compounds stacked together in an irregular pattern [48,49]. The combination of EDS and EELS imaging (shown in Fig. 3) suggests that there is an SEI bilayer with segregation of organic and inorganic phases, but also that these layers are separated to some extent into particulate domains.

The surface distribution of elements in the SEI can be determined qualitatively through SAM, as shown in Fig. S4. C and O are present in the SEI, so they are present over most of the SAM maps. However, in the 25 °C at Gen2 and the 70 °C at GenF samples, the C and O do not completely cover the map; there are domains that have different concentrations of these elements. In the 70 °C Gen2 and the 25 °C GenF samples, there is a more uniform distribution of these two elements.

One drawback of XPS is the relatively low lateral resolution, which makes it difficult create spatial maps of the compounds in a composite electrode sample (where the SEI can be heterogeneous on the nanoscale). SAM provides high-resolution mapping, but it generally provides no information on chemical states, and like XPS, it is insensitive to bulk compositional variations. As discussed previously, STEM characterization is a useful tool for making elemental maps at relevant length scales, and it probes more deeply within samples than other techniques. In some cases, these maps can be used to study the location and size of different compounds in the SEI by correlating between elements. For example, in the STEM-EELS mapping (Fig. 3(b)), Li and F were found to be in nearly the same location, and there were not any large domains of either element located independently of the other. The existence of LiF is well documented in LiB SEIs, so it can reasonably be concluded that these overlaps represent regions of LiF [19,49]. The small LiF domains (around 50–150 nm in width) are consistent with previous reports [17].

4.3. Connecting electronic resistivity to composition

Previous SSRM work on individual inorganic SEI components found that LiF is one of the most highly electrically resistive components, with a resistivity of 2.18×10^{10} Ω-cm for a pure film [50]. In comparison, pure Li_2CO_3 has a resistivity on the order of 10^4 Ω-cm at room temperature [51]. As discussed above, we determined the presence of LiF through XPS and STEM-EELS. The quantity of each species can be estimated from XPS peak intensities, but there are several factors that could introduce error into this analysis. XPS likely does not analyze the whole of the SEI through its thickness, and the SEI composition varies with depth. In contrast, STEM-EDS does analyze the whole SEI, but does not provide a quantitative value for LiF content. When the F content from each technique is compared, the values do not match due to varying interaction depths, but they do follow the same relative ranking. Based on this, we assume that measuring LiF via XPS is a reasonable method for analyzing resistivity trends. Both the average resistivity of the SEI domain and the maximum resistivity of each map were compared to the estimated LiF content, shown in Fig. 6. The maximum resistivity was directly proportional with the LiF content. From the STEM-EELS images, we observed that the LiF was in the form of particles on the order of 80–100 nm in diameter. The images were 10-μm-square and contained 128 rows with 128 data points each, meaning that each pixel represents approximately 80 nm by 80 nm of surface area. The SSRM probe has a nominal diameter of 200 nm, so it is possible for the probe not to measure individual LiF particles, particularly if the LiF content is low and the particles are not clustered together. The measured resistivity is also impacted significantly by surrounding materials with different resistivities. This particle morphology is likely the reason that the maximum measured resistivity increases with LiF content, as higher LiF content can increase LiF particle clustering.

The average SEI resistivity appears to be less closely related to the LiF content. The Gen2 samples both showed a higher average resistivity than the GenF samples, although there is not a clear relationship between temperature and average resistivity. The variation in the relationship between maximum and average resistivity indicates that LiF is not solely responsible for a resistive SEI; this is to be expected, as the SEI is heterogeneous and contains different compounds with different resistivities [50]. However, increasing LiF content may be one method of increasing SEI resistivity to effectively block parasitic electrochemical

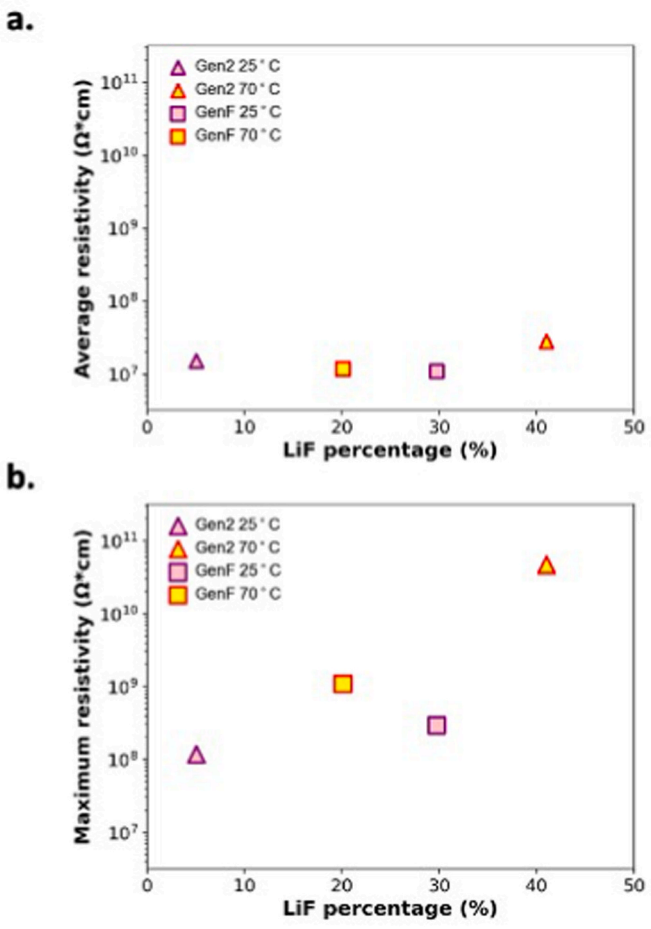

Fig. 6. LiF content, as determined by XPS, compared to (a) average SEI resistivity, showing a slight correlation, and (b) maximum SEI resistivity, showing a more significant relationship between LiF content and increased resistivity.

reactions. Simultaneously, maintaining high Li^+ ion conductivity should also be considered [52].

Based on the previously discussed data demonstrating a bilayer SEI structure, we can assume that the SEI resistivity is not consistent through its thickness. Previous studies have drawn inconsistent conclusions about the resistivity of outer versus inner SEI layers [53]. It is worth noting that the general knowledge about material resistivity may not fully apply to SEI, as grain size and defect configurations—which can affect the real resistivity of SEI components—are different from those found in materials with large grain sizes or single crystalline materials. Therefore, the average resistivity of the SEI may be a less relevant property than the maximum resistivity, as the actual volume of the inner layer and the LiF is independent of the SEI's average resistivity and its effectiveness in blocking parasitic reactions. Because LiF is not the only compound controlling SEI resistivity, future studies should conduct further chemical and SSRM analysis to study other inorganic and organic species. Si-containing species such as silicon oxide and lithium silicates are also highly resistive and may be studied by analyzing the Si content present in the SEI [50]. These species and others (e.g. lithium hexafluorsilicate) are of particular interest for Si electrode optimization, as they may play a role in poor SEI stability [54]. Organic species that likely dominate the outer layer of the SEI and directly contact the electrolyte may play an important role in protecting the electrode active materials from parasitic reactions.

5. Conclusion

Understanding the SEI in composite electrode systems can be challenging due to the complex three-dimensional structure, heterogeneity across the sample surface, and general issues with samples, such as roughness. Here, we demonstrate approaches for combining and comparing several different characterization techniques. We showed that elemental analysis techniques have considerable variability due to sample interactions and element sensitivities, which should be considered when measuring composition via any single technique. Combining multiple techniques can help provide a more comprehensive understanding of the SEI and can help correlate its chemical composition to other physical properties, like resistivity. This insight can guide electrode and electrolyte design to improve cell performance.

In this study, we found the SEI forms a bilayer and fully covers the electrode surface, but the thickness varies considerably, from 10 to 50 nm on different particles. We also determined that most of the Li in the SEI is in LiF and is present in clusters in the inner layer, rather than evenly distributed. We correlated maximum SEI resistivity with LiF content but found no relationship between LiF concentration and average SEI resistivity, suggesting that the relationship between LiF and SEI resistivity is complex, particularly in a heterogeneous SEI, and additional studies on the role of LiF in electrode passivation are required. Finally, we found an inverse relationship between concentration of LiF and $LiCO_3$ on the SEI surface, suggesting it may be possible to tune LiF content more precisely by decreasing $LiCO_3$. Further study is warranted on the relationship between other SEI compounds and resistivity, as well as the impacts of SEI heterogeneity and component distribution on overall resistivity and passivation.

CRediT authorship contribution statement

Zoey Huey: Conceptualization, Investigation, Formal analysis, Writing – original draft, Visualization. **Yeyoung Ha:** Conceptualization, Investigation, Writing – review & editing. **Sarah Frisco:** Investigation, Formal analysis, Visualization. **Andrew Norman:** Investigation, Formal analysis, Visualization. **Glenn Teeter:** Investigation, Formal analysis, Visualization. **Chun-Sheng Jiang:** Supervision. **Steven C. DeCaluwe:** Writing – review & editing, Supervision.

Declaration of competing interest

The authors declare that they have no known competing financial interests or personal relationships that could have appeared to influence the work reported in this paper.

Data availability

Data will be made available on request.

Acknowledgements

This work was authored in part by the National Renewable Energy Laboratory, operated by Alliance for Sustainable Energy, LLC, for the U. S. Department of Energy (DOE) under Contract No. DE-AC36-08GO28308. Funding provided by U.S. Department of Energy's Vehicle Technologies Office under the Silicon Consortium Project, directed by Brian Cunningham and managed by Anthony Burrell. The views expressed in the article do not necessarily represent the views of the DOE or the U.S. Government. The U.S. Government retains and the publisher, by accepting the article for publication, acknowledges that the U.S. Government retains a nonexclusive, paid-up, irrevocable, worldwide license to publish or reproduce the published form of this work, or allow others to do so, for U.S. Government purposes. Electrodes provided by Steve Trask and the Cell Analysis, Modeling and Prototyping Facility at Argonne National Laboratory. FIB lift out samples were created by Patrick Walker at the National Renewable Energy Laboratory.

Appendix A. Supplementary data

Supplementary data to this article can be found online at https://doi.org/10.1016/j.jpowsour.2023.232804.

References

[1] K. Feng, M. Li, W. Liu, A.G. Kashkooli, X. Xiao, M. Cai, Z. Chen, Small 14 (2018).
[2] P. Li, J.Y. Hwang, Y.K. Sun, ACS Nano 13 (2019) 2624–2633.
[3] M.N. Obrovac, L.J. Krause, J. Electrochem. Soc. 154 (2007) A103–A108.
[4] E. Peled, S. Menkin, J. Electrochem. Soc. 164 (2017) A1703–A1719.
[5] U. Kasavajjula, C. Wang, A.J. Appleby, J. Power Sources 163 (2007) 1003–1039.
[6] H.G. Steinruck, C. Cao, G.M. Veith, M.F. Toney, J. Chem. Phys. 152 (2020), 084702.
[7] S.P.V. Nadimpalli, V.A. Sethuraman, S. Dalavi, B. Lucht, M.J. Chon, V.B. Shenoy, P. R. Guduru, J. Power Sources 215 (2012) 145–151.
[8] C.-H. Yim, S. Niketic, N. Salem, O. Naboka, Y. Abu-Lebdeh, J. Electrochem. Soc. 164 (2016) A6294–A6302.
[9] R. Marom, S.F. Amalraj, N. Leifer, D. Jacob, D. Aurbach, J. Mater. Chem. 21 (2011) 9938–9954.
[10] M.-S. Balogun, Y. Luo, W. Qiu, P. Liu, Y. Tong, Carbon 98 (2016) 162–178.
[11] L. Saei Fard, N.S. Peighambardoust, H.W. Jang, A. Dehghan, N. Nehzat Khosh Saligheh, M. Iranpour, M. Isvand Rajabi, J. Compos. Compd. 2 (2020) 138–146.
[12] S.D. Beattie, D. Larcher, M. Morcrette, B. Simon, J.M. Tarascon, J. Electrochem. Soc. 155 (2008) A158–A163.
[13] A. Ghamlouche, M. Müller, F. Jeschull, J. Maibach, J. Electrochem. Soc. 169 (2022).
[14] J.D. McBrayer, M.-T.F. Rodrigues, M.C. Schulze, D.P. Abraham, C.A. Apblett, I. Bloom, G.M. Carroll, A.M. Colclasure, C. Fang, K.L. Harrison, G. Liu, S. D. Minteer, N.R. Neale, G.M. Veith, C.S. Johnson, J.T. Vaughey, A.K. Burrell, B. Cunningham, Nat. Energy 6 (2021) 866–872.
[15] B. Li, X. Gao, J. Li, C. Yuan, Environ. Sci. Technol. 48 (2014) 3047–3055.
[16] L. Benitez, D. Cristancho, J.M. Seminario, J.M. Martinez de la Hoz, P.B. Balbuena, Electrochim. Acta 140 (2014) 250–257.
[17] W. Huang, H. Wang, D.T. Boyle, Y. Li, Y. Cui, ACS Energy Lett. 5 (2020) 1128–1135.
[18] T. Jaumann, J. Balach, M. Klose, S. Oswald, U. Langklotz, A. Michaelis, J. Eckert, L. Giebeler, Phys. Chem. Chem. Phys. 17 (2015) 24956–24967.
[19] J. Tan, J. Matz, P. Dong, J. Shen, M. Ye, Adv. Energy Mater. 11 (2021).
[20] F. Aupperle, N. von Aspern, D. Berghus, F. Weber, G.G. Eshetu, M. Winter, E. Figgemeier, ACS Appl. Energy Mater. 2 (2019) 6513–6527.
[21] X. Chen, X. Li, D. Mei, J. Feng, M.Y. Hu, J. Hu, M. Engelhard, J. Zheng, W. Xu, J. Xiao, J. Liu, J.G. Zhang, ChemSusChem 7 (2014) 549–554.
[22] Y. Yin, E. Arca, L. Wang, G. Yang, M. Schnabel, L. Cao, C. Xiao, H. Zhou, P. Liu, J. Nanda, G. Teeter, B. Eichhorn, K. Xu, A. Burrell, C. Ban, ACS Appl. Mater. Interfaces 12 (2020) 26593–26600.

[23] L. Martin, H. Martinez, M. Ulldemolins, B. Pecquenard, F. Le Cras, Solid State Ionics 215 (2012) 36–44.
[24] M. Salah, P. Murphy, C. Hall, C. Francis, R. Kerr, M. Fabretto, J. Power Sources 414 (2019) 48–67.
[25] C. Stetson, T. Yoon, J. Coyle, W. Nemeth, M. Young, A. Norman, S. Pylypenko, C. Ban, C.-S. Jiang, M. Al-Jassim, A. Burrell, Nano Energy 55 (2019) 477–485.
[26] H.J. Mathieu, Auger electron spectroscopy, in: J.C. Vickerman, I.S. Gilmore (Eds.), Surface Analysis : the Principal Techniques, John Wiley & Sons, Incorporated, Germany, 2009, pp. 9–46.
[27] B.D. Ratner, D.G. Castner, Electron spectroscopy for chemical analysis, in: J. C. Vickerman, I.S. Gilmore (Eds.), Surface Analysis: the Principle Techniques, John Wiley & Sons, Inorporated, Germany, 2009, pp. 47–112.
[28] D.B. Williams, C.B. Carter, Transmission Electron Microscopy Part 1: Basics, second ed. ed., Springer, 2009.
[29] S.H. Kim, Y.S. Kim, W.J. Baek, S. Heo, S. Han, H. Jung, J. Power Sources 407 (2018) 1–5.
[30] P. Verma, P. Maire, P. Novák, Electrochim. Acta 55 (2010) 6332–6341.
[31] A.E. Goode, A.E. Porter, M.P. Ryan, D.W. McComb, Nanoscale 7 (2015) 1534–1548.
[32] K.N. Wood, G. Teeter, ACS Appl. Energy Mater. 1 (2018) 4493–4504.
[33] P. Eyben, W. Vandervorst, D. Alvarez, M. Xu, M. Fouchier, Probing semiconductor technology and devices with scanning spreading resistance microscopy, in: S. Kalinin, A. Gruverman (Eds.), Scanning Probe Microscopy: Electrical and Electromechanical Phenomena at the Nanoscale, Springer New York, New York, NY, 2007, pp. 31–87.
[34] F.M. Smits, Bell Syst. Tech. J. 37 (1958) 711–718.
[35] C. Stetson, Z. Huey, A. Downard, Z. Li, B. To, A. Zakutayev, C.S. Jiang, M.M. Al-Jassim, D.P. Finegan, S.D. Han, S.C. DeCaluwe, Nano Lett. 20 (2020) 8081–8088.
[36] S.H. Kim, Y.S. Kim, W.J. Baek, S. Heo, D.J. Yun, S. Han, H. Jung, ACS Appl. Mater. Interfaces 10 (2018) 24549–24553.
[37] S.Y. Park, W.J. Baek, S.Y. Lee, J.A. Seo, Y.-S. Kang, M. Koh, S.H. Kim, Nano Energy 49 (2018) 1–6.
[38] Y. Ha, D.P. Finegan, A.M. Colclasure, S.E. Trask, M. Keyser, Electrochim. Acta 394 (2021).
[39] M. Seah, I. Gilmore, G. Beamson, Surf. Interface Anal. 26 (1998) 642–649.
[40] A.G. Shard, J. Vac. Sci. Technol., A 38 (2020), 041201.
[41] A. Jablonski, C.J. Powell, J. Electron. Spectrosc. Relat. Phenom. 281 (2017) 1–2.
[42] D.E. Newbury, N.W. Ritchie, Scanning 35 (2013) 141–168.
[43] L.E. Davis, N.C. MacDonald, P.W. Palmber, G.E. Riach, R.E. Weber, Handbook of Auger Electron Spectroscopy, second ed., Physical Electronics Division, Perkin-Elmer Corporation, 1976.
[44] G.M. Veith, M. Doucet, R.L. Sacci, B. Vacaliuc, J.K. Baldwin, J.F. Browning, Sci. Rep. 7 (2017) 6326.
[45] K. Schroder, J. Alvarado, T.A. Yersak, J. Li, N. Dudney, L.J. Webb, Y.S. Meng, K. J. Stevenson, Chem. Mater. 27 (2015) 5531–5542.
[46] S.J. An, J. Li, C. Daniel, D. Mohanty, S. Nagpure, D.L. Wood, Carbon 105 (2016) 52–76.
[47] C.H. Lee, J.A. Dura, A. LeBar, S.C. DeCaluwe, J. Power Sources 412 (2019) 725–735.
[48] M. Boniface, L. Quazuguel, J. Danet, D. Guyomard, P. Moreau, P. Bayle-Guillemaud, Nano Lett. 16 (2016) 7381–7388.
[49] S.K. Heiskanen, J. Kim, B.L. Lucht, Joule 3 (2019) 2322–2333.
[50] S.D. Han, K.N. Wood, C. Stetson, A.G. Norman, M.T. Brumbach, J. Coyle, Y. Xu, S. P. Harvey, G. Teeter, A. Zakutayev, A.K. Burrell, ACS Appl. Mater. Interfaces 11 (2019) 46993–47002.
[51] J. Mizusaki, H. Tagawa, K. Saito, K. Uchida, M. Tezuka, Solid State Ionics 53–56 (1992) 791–797.
[52] J. Pan, Y.-T. Cheng, Y. Qi, Phys. Rev. B 91 (2015).
[53] C. Stetson, Y. Yin, C.-S. Jiang, S.C. DeCaluwe, M. Al-Jassim, N.R. Neale, C. Ban, A. Burrell, ACS Energy Lett. 4 (2019) 2770–2775.
[54] C. Yu, X. Chen, Z. Xiao, C. Lei, C. Zhang, X. Lin, B. Shen, R. Zhang, F. Wei, Nano Lett. 19 (2019) 5124–5132.